Mechatronics 19 (2009) 29–41

Contents lists available at ScienceDirect

Mechatronics

journal homepage: www.elsevier.com/locate/mechatronics

Design and control of a brushless DC limited-angle torque motor with its application to fuel control of small-scale gas turbine engines

Ching-Chih Tsai *, Shui-Chun Lin, Hsu-Chih Huang, Yu-Ming Cheng

Department of Electrical Engineering, National Chung Hsing University 250, Kuo-Kuang Road, Taichung 40227, Taiwan

ARTICLE INFO

Article history:
Received 15 April 2006
Accepted 7 July 2008

Keywords:
Actuator
Fuel control
Limited-angle torque motor (LATM)
PID control
Small-scale gas turbine engine

ABSTRACT

This paper presents techniques for design and control of a brushless direct-current (DC) limited-angle torque motor (LATM) with its application to fuel control of gas turbine engines. Given the desired specifications, a two-pole brushless DC LATM with a toroidally wound armature is designed using selected ferromagnetic material and rare-earth permanent magnets; its electromagnetic characteristics is then computationally found and well tuned using the finite element method (FEM) in order to ensure whether the design meets the performance specifications. To achieve the simple and inexpensive semi-closed-loop fuel control, a robust position controller (including a proportional-integral-derivative (PID) controller with a prefilter) is synthesized for providing the required positioning performance for the developed motor, thereby achieving an inexpensive semi-closed-loop fuel control. A closed-loop fuel controller associated with the proposed position controller and a flow meter is then proposed based on multi-loop control structure in order to achieve required linear input–output relationship. All the proposed fuel control laws were implemented using a stand-alone single-chip digital signal processor (DSP). Experimental results are conducted to show the efficacy and usefulness of the developed limited-angle torque motor with its application to an experimental gas turbine fuel control test platform.

1. Introduction

The limited-angle torque motor (LATM) is an electromagnetic rotary actuator which converts small electrical current into limited angular movement, producing torque through a limited rotation angle of normally much less than ±180°. In order to accommodate the requirements of various applications, several different physical structures and configurations of LATMs have been presented based on their different working principles. For examples, the torque motors developed in [1–3] are all based on the same polarized reluctance principle, Zhang et al. [4] constructed an LATM according to the Laws' relay principle, Krishna and Kannan [5] designed and implemented a special type of brushless DC motor called brushless DC limited-angle torque motor, and Du et al. [6] presented a novel LATM where the stator is made by two pairs of permanent magnets and the rotor is composed of the winding. Common features of such motors hinge on their small physical sizes, quick response times and high flux density permanent magnets, even rare-earth permanent magnets. These torque motors have been widely used in the areas of aerospace and space equipment, optical scanning systems and even any drive systems that require limited mechanical rotation, ranging from the simple ON–OFF control of servo valves to the accurate tracking control of a reference signal.

The brushless DC LATM has been considered as a direct-drive and frameless actuator which is designed for any positioning systems requiring limited-angle operation. The brushless DC LATM has the similar structure of a typical brushless DC motor, namely that the stator supports the armature winding and the field magnets are mounted on the rotor. However, this type of limited-angle torque motor is much more inexpensive because the armature windings are connected for single phase, thereby eliminating the need of using the electronic switching to carry out commutation action. Furthermore, such a motor has been shown particularly useful in both aerospace and space applications with the performance benefits of high torque/power ratio, high reliability, low cost, precise positioning and maintain free operations.

There are few published materials on the design of the brushless DC LATM, in part due to the particular nature of its design and special applications and in part because of commercial confidentiality. In general, the structures of the brushless DC LATMs can be classified into two categories: slotted wound armature and toroidally wound armature. Krishna and Kannan [5] compared these two types of brushless DC LATM designs, and found that although the slotted wound LATMs have higher torque constant, they are with greater magnetic friction and iron losses, and even torque ripple due to cogging; on the contrary, the toroidally wound

* Corresponding author. Tel.: +886 4 22859351; fax: +886 4 22856232.
E-mail address: cctsai@dragon.nchu.edu.tw (C.-C. Tsai).

0957-4158/$ - see front matter © 2008 Elsevier Ltd. All rights reserved.
doi:10.1016/j.mechatronics.2008.07.003

LATMs do not have the cogging problem because of constant reluctance path and relatively large air gap, and they were selected for the specific space applications. Furthermore, the authors in [5] proposed two-pole and four-pole toroidally wound brushless DC LATMs with the rotors made by samarium cobalt magnets (Sm_2CO_5); they concluded that the toroidally wound armature along with rare-earth permanent magnet rotor seems to be a good solution for high-performance limited rotation applications.

For the brushless DC LATM design issues in the aircraft's and spacecraft's applications, the selection of the permanent magnets is another significant problem. Rao [7] discussed with the Alnico alloy and expounded its applications. Tufts [8] offered the way to select appropriate and adequate permanent magnets, Mhango [9] presented the reports about the benefits of new rare-earth magnets for aircraft applications, and Petrie [10] provided a broad overview of permanent magnet materials with their significant advantages and disadvantages. For example, in comparison with samarium cobalt magnets, Neodymium–ferrite–boron magnets have the advantages of greater peak torque capability, higher energy product, higher coercive force, more compactness, and lower energy cost, but posses the disadvantages of bad performance varying with temperatures and lower service temperature. Furthermore, Pal [11] presented comparative study of the design and development of direct drive brushed and brushless DC motors with samarium cobalt, neodymium–iron–boron and ceramic magnets, Oman [12] discussed the design considerations for permanent magnet motors and Jabbar et al. [13] investigated permanent magnet motors for brushless operation. Yoon [14] considered stator design of a brushless DC motor for robust rotor position detection in inductive sense start-up. Zheng et al. [15] presented the design and implementation of a super high-speed cryogenic permanent magnet synchronous motor; this kind of motor has a similar configuration of the brushless DC LATM. Komori and Yamane [16] developed a millimeter-sized cylindrical rotor that makes a very quick response because of its small mass (95 mg). In addition, the use of the finite element method (FEM), called ANSYS, has been shown effort-saving and effective in designing the brushless DC LATMs in [5]. Other finite element methods for motors design have also been reported in [17,18].

Moreover, the recent rapid and revolutionary advent of power electronics and microelectronics has already made digital motor controllers possible to implement and apply well-developed sophisticated control theories. Up to now, digital signal processors (DSPs) have been used to most applications in [19,20]. Brown et al. [21] proposed the design of the DSP subsystem for gas turbine engine. Due to the powerful computation abilities and high sampling rate, DSPs are much easier to perform the desired function and control algorithms in real time than the conventional microcomputers and analog controllers. With the advantages, digital signal processors with military specifications have become prevalent in numerous aerospace and space applications.

Although the brushless DC LATMs are not new for practitioners and engineers in the fields of aerospace and space applications, this article attempts to revisit the design of the toroidally wound brushless DC LATM with the rotor made by specific rare-earth permanent magnets, neodymium–ferrite–boron (NdFeB), and develop simple but robust position controllers using digital signal processing technology, thereby resulting in more compact, powerful and reliable motors and their position controllers. The proposed motor along with the digital controllers will be then demonstrated by means of its application to a fuel control system in a small-scale gas turbine engine. Small-scale gas turbine engines have become increasingly important for specific aircrafts and miniature rotorcrafts, such as unmanned airborne aircraft, missiles, miniature helicopters and power generators [22,23]. The fuel control systems for such small-scale gas turbine engines are considered as key components because they significantly affect the performance and reliability of the small-scale gas turbine engines. Generally speaking, such a fuel control system is typically equipped with a low-cost but very reliable brushless DC LATM, a fuel controller and a simple valve with associated components. The proposed brushless DC limited-angle torque motor along with the robust DSP-based controllers will be shown useful in such a small-scale aviation subsystem due to its quick response, accurate positioning and robustness against possible parameter variations and exogenous disturbances.

The main contributions of the paper are threefold: (i) a new brushless DC LATM with required design specifications is successfully developed utilizing the analytical approach and the finite element method, called Flux2D. Furthermore, the developed motor is proven satisfactory and consistent through experimental data. Unlike the armature winding design in [5], the gaps between any two serial windings are especially designed in order to generate the required constant output torque within the operation range of the motor. (ii) The single-chip DSP-based robust position controller is successfully designed and implemented to achieve semi-closed-loop fuel control in a small-scale gas turbine engine fuel control test platform. (iii) With a flowmeter, the overall closed-loop fuel control system is constructed to carry out the required linear relationship between the steady-state controlled flow rates and the corresponding commands. The proposed motor design and control methods are expected to be efficient and pragmatic for other aerospace and space applications requiring aforementioned advantages.

The remainder of this paper is organized as follows. Section 2 is dedicated to the design and implementation of the brushless DC LATM utilizing the analytical approach and the finite element method (FEM)-based CAD program; particular attention is paid to the performance evaluation of the proposed motor with an analog proportional controller. In Section 3, the small-scale gas turbine fuel control system is briefly described and the low-cost, robust semi-closed-loop fuel controller is designed using the two-degree-of-freedom control structure. To eliminate the nonlinearity caused by the fuel valve, the closed-loop fuel controller with a flowmeter is also synthesized. In Section 4, experimental results are conducted to verify the efficacy and usefulness of the proposed small-scale gas turbine fuel control system. Section 5 concludes the paper.

2. Brushless DC LATM design and performance evaluation

This section is concerned with the techniques for design and implementation of the brushless DC LATM. The type of torque motor is specially designed for the small-scale gas turbine fuel control modules with performance benefits of direct drive, high reliability, high torque, accurate positioning and maintenance free operation. The high reliability comes from its simple and rugged structure, which uses a two-pole permanent-magnet rotor and a solid-core stator with a toroidally wound armature. The high torque results from the use of rare-earth permanent magnets and numerous conductors over one pole. The accurate position capability can be easily achieved using the proposed robust position controller together with the high-resolution potentiometer mounted on the rotor shaft. The maintenance free operation is due to no commutation brushes and no switching circuitry.

2.1. Specifications

The drive motor for this application should meet the specifications throughout the life time of the small-scale gas turbine fuel control modules. Moreover, the motor's output torque should remain constant, namely that the output torque is independent of

the rotor's position or velocity. To achieve desired performance required in the small-scale gas turbine fuel system, the brushless DCLATM must satisfy the following specifications: (1) the physical size is as small as possible; (2) the maximum torque is not less than 1.3 kg cm; (3) the limited angular rotation or the constant torque region (>80% of the peak torque) is limited to ±60°; (4) the input voltage ranges from 0V DC to 12 V DC; (5) the maximum armature current is 800 mA; (6)the bandwidth requirement for closed-loop position control is greater than 5 Hz; (7) the weight of the motor is less than 600 g.

2.2. Physical configuration

As depicted in Fig. 1a, the proposed torque motor has a toroidally wound armature in the stator and a two-pole permanent-magnet rotor. The four DC windings in the stator are connected for single phase such that a simple DC current driving circuitry is employed for the motor. Fig. 1b shows the physical size of the designed torque motor. The basic principle of the motor is briefly described as follows. The interaction of two magnetic fields created by the permanent magnets and the stator windings generates an electromagnetic torque. Thus, the rotor will be attracted or propelled by the magnetic field of the exciting stator. By applying appropriate DC armature current to the stator windings, the rotor will be controlled to the desired position in one direction and vice versa. If a closed-loop control policy through position feedback is used, then the rotor will be forced to the required position in a desired manner.

2.3. Stator design

The subsection is concerned with how to select an appropriate magnetic material for the stator core and how to assemble the toroidal type armature. In general, a good ferromagnetic material candidate must have low hysteresis loss, low core cavity and low retentivity. Aside from hysteresis and coercivity, the saturation value of the flux density of the material is also noticeably important. Table 1 lists typical magnetic properties of four commonly used ferromagnetic materials. As can be seen in Table 1, both the saturation value and permeability of the alloy Fe–Co are superior to others and the alloy has the minimum level of tolerance for the flux density. Note that this saturation value is smaller than that of the magnetic flux generated by the rotor, or the flux provided from the rotor will have flux leakage outside of the stator core. In order to avoid the flux leakage and the hysteresis loss problem, the alloy Fe–Co is chosen as the magnetic material for the stator core.

As Fig. 2 shows, the armature stator assembly for the two-pole brushless DC LATM is composed of four coils toroidally wound on the solid core without slots. Such a stator gives many benefits, such as high reliability due to contactless electronic switching, high torque because of possible maximum conductors over a pole, and ease of maintenance. Fig. 2a presents the schematic diagrams of the four stator windings, each of which has 256 turns of conductors wrapped around the stator core, where each conductor is with the diameter of 0.32 mm. Fig. 2a also presents the cross-section of a physical stator winding closely mounted on a cylindrical iron core. Moreover, each coil has multilayered winding wound over an arc length of approximately 79°. The four stator windings are connected in series such that the resulting current directions in the windings are shown in Fig. 1a and the torque developed by all the coils is additive. The stator windings have the total resistance of approximately 16.5 ohms (Ω) and the total inductance of 22 mH. It is worth noting that, unlike the armature winding design in [5], the gaps between any two serial windings are especially designed in order to generate the required constant output torque within the operation range of the motor. The toroidal armature core is accurately mounted on the armature housing and is then encapsulated with a thermally conductive epoxy potting compound which keeps the windings from damage and holds them in place.

2.4. Permanent magnet rotor design

Fig. 2b illustrates the physical diagram of the designed rotor that is composed of two axially magnetized permanent magnets: one magnet holder and one rotary shaft. The two-pole permanent magnets are employed to produce magnetic flux in the annular air gap of 1.25 mm. The magnets and magnet holder are fixed with an adhesive compound.

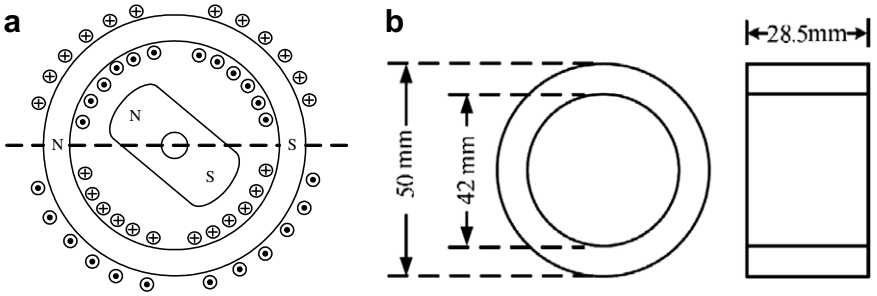

Fig. 1. (a) Conceptual configuration and current directions of the torque motor. (b) Physical size of the designed torque motor.

Table 1
Properties of four typical magnetic materials

Material	Permeability		Hysteresis loss. (Ergs per cm^3 per cycle)	Maximum induction (gausses)	Coercive force (Oersteds)	Saturation value (gausses)	Density (g/cm^3)	Hardness (HRB)
	Init.	Max.						
0.5% Si steel	280	3000	2300	10,000	0.90	20,500	7.75	43
3.0% Si steel	290	8000	1600	10,000	0.70	20,900	7.65	100
Ingot iron	150	5000	2700	10,000	1.00	21,400	7.88	63
Fe–Co alloy	800	70,000	1500	21,000	0.23	24,000	8.15	77

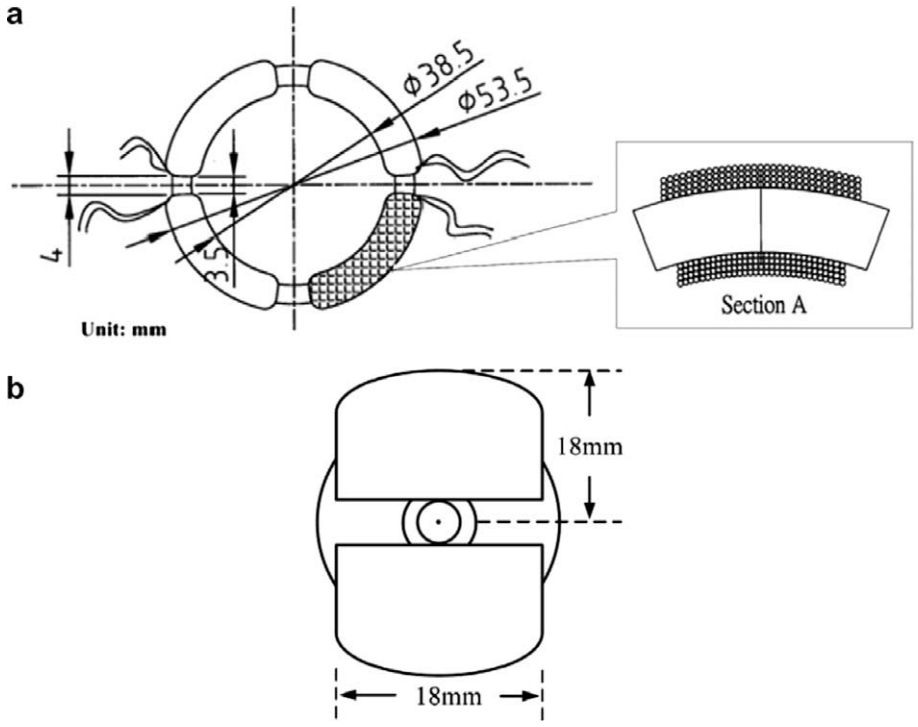

Fig. 2. (a) Schematic diagram of the toroidally wound stator assembly. (b) Physical size of the permanent magnet rotor assembly.

2.4.1. Selection of permanent magnets

Before selecting permanent magnets for the rotor, the understanding of the properties of the most useful permanent magnets is a must. Among the most useful permanent magnets are hard ferrite, alnico, samarium cobalt (SmCo) and neodymium–ferrite–boron (NdFeB). Table 2 compares the aforementioned permanent magnets in terms of physical and magnetic characteristics, in which B_r represents the residual flux (unit: T), H_c the coercivity force (unit: kA/m), and BH_{max} the maximum of the product of the magnetic flux and magnetic intensity (unit: kJ/m^3). For the temperature adaptability and the need of high peak torque capability, both samarium cobalt and neodymium–ferrite–boron (NdFeB) magnets are two good candidates for the rotor designed over the temperature range from −15 °C to 80 °C. Furthermore, NdFeB permanent magnets give the significant advantages of greater peak torque, higher energy product, higher coercive force, allowing larger air gap, less weight, less physical size and less energy cost while compared to samarium cobalt magnets. Hence, NdFeB permanent magnets are the chosen magnets for the rotor. Worthy of mention is that particular protective coating is used to overcome with the impressionable corrosion problem of NdFeB permanent magnets through the life time of the motor.

2.4.2. Air-gap magnetic flux density generated by the rotor

Each pole surface of the rotor has an arc length of approximately 60° especially fitted to the requirement of the limited angular movement of ±60°. From the Ampere's law around the flux path, one obtains

$$\oint \vec{H}\,\mathrm{d}\vec{l} = H_m l_m + H_g l_g = 0 \tag{1}$$

where H_m and l_m represent, respectively, the magnetic intensity and the length of the magnetic path in the stator core, and H_g and l_g denote, respectively, the magnetic intensity and the length of the magnetic path in the air gap. By assuming that no magnetic saturation occurs, the linear B–H characteristics of the permanent magnet materials are given by

$$B_m = B_r + \mu_0 \mu_r H_m \tag{2}$$

where B_m and B_r are the magnetic flux density in the stator and the residual magnetic flux density in the air gap; μ_0 and μ_r are the relative permeability in the free space and in the stator core, respectively. The continuity property of the magnetic flux Φ yields

$$\Phi = B_m A_m = B_g A_g \tag{3}$$

Table 2
Comparisons of the four commercial permanent magnets in terms of physical and magnetic properties where BH_{max} represents the maximum of the product of the magnetic flux and magnetic intensity (unit: kJ/m^3)

Magnetic material	Residual flux, B_r (T)	Coercivity force, H_c (kA/m)	BH_{max} (kJ/m^3)	Temperature coefficient of remanence (% per °C)	Temperature coefficient of coercivity (% °C)	Maximum operating temperature (°C)	Density (g/cm^3)
Ferrite	0.400	295	29	−0.200	+0.400	250	4.9
Alnico	1.070	50	40	−0.020	+0.020	500	7.3
SmCo	0.920	705	170	−0.045	−0.250	250	8.4
NdFeB	1.150	840	240	−0.100	−0.700	150	7.4

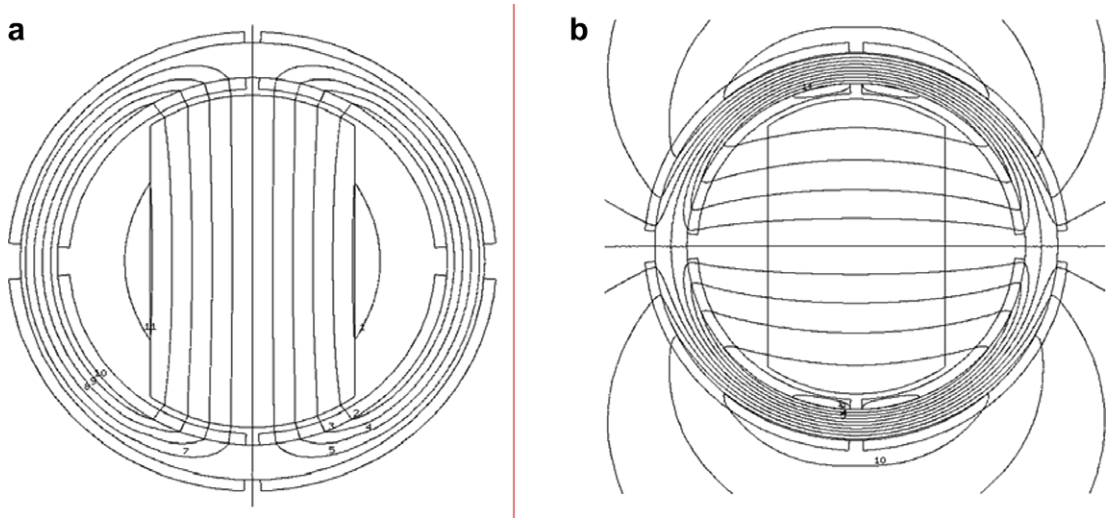

Fig. 3. (a) Flux distribution of the permanent magnet rotor. (b) Flux distribution of the stator with the input current of 800 mA.

Substituting (3) into (2) gives

$$\left(\frac{B_m - B_r}{\mu_r \mu_0}\right) l_m + \frac{B_g}{\mu_0} l_g = 0 \tag{4}$$

Elimination of B_m from (2) and (3) gives the resulting air-gap flux density

$$B_g = \frac{B_r}{\left(\frac{A_g}{A_m} + \mu_r \frac{l_g}{l_m}\right)} \tag{5}$$

From (5), it follows that dimension of the torque motor including the rotor and the stator core can be designed to obtain the desired air-gap flux density in the air gap or inside the stator core.

2.5. Torque formula and verification using flux2D

This subsection is dedicated to finding a torque formula of the motor. Since this type of torque motor with a pillared rotor and an annular stator is very exceptional, it is very difficult to find an exactly analytical torque formula. Hence, a simple and approximate torque formula is proposed for the motor; the formula is then verified using the commercial computer aided design package, called Flux2D. Since the motor has an almost step-like air-gap flux density in the periphery of the rotor, the electromagnetic torque can be derived by the Fleming's left-hand rule and electromagnetic force. Thus, the total resultant electromagnetic torque of the motor is approximately obtained from

$$T \approx k2rnilB_g \tag{6}$$

where k is a constant parameter, r is the radius of the rotor, i and l denote, respectively, the current and the effective length of each conductor, and n represents the total effective turns of the conductors over one rotor's pole. Note that the parameter n remains almost constant within the allowed operating range of the rotor. It reveals from Eq. (6) that the resultant torque is proportional to the armature current within the specific range of the allowable angle, and the torque will be kept constant if a fixed input DC current is applied.

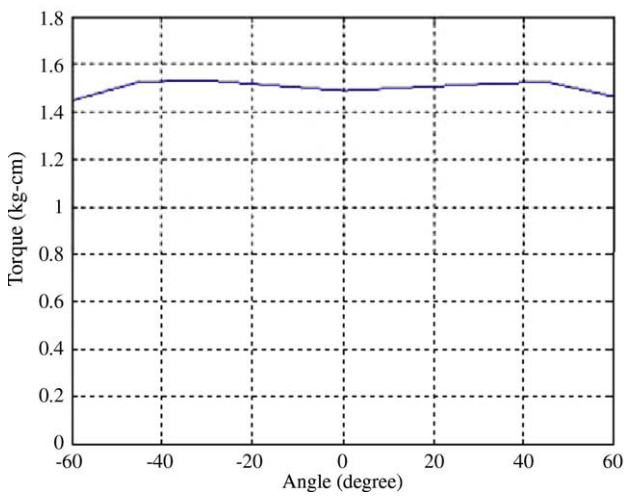

Fig. 4. Simulation result of the motor's torque over the limited angular movement when the armature current is 800 mA.

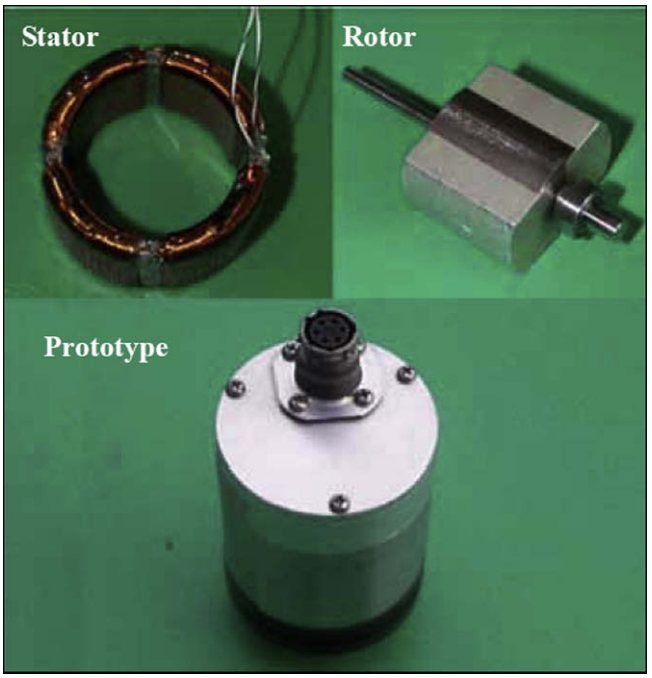

Fig. 5. Pictures of the designed stator, rotor and torque motor.

For verifying the validity of the torque formula (6), a powerful magnetic circuit analysis tool, called Flux2D, is used to proceed with computational torque analysis and the design refinement for the motor. Using the standard procedure to input the geometry, physical property and input current of the motor, one can simulate the torque and the magnetic flux density generated respective by the stator's windings and the rotor via the finite element method in the package Flux2D. Fig. 3, respectively, depicts the resultant flux distributions of the permanent magnet rotor and the stator when the rotor is at the position in Fig. 3a. The results in Fig. 3a and b indicate that two magnetic fields caused by the rotor and the stator are almost perpendicular, thus generating required electromagnetic torque. The result in Fig. 4 reveals that given the maximum input current, the simulated torque remains approximately constant at the entire constrained rotor's angles.

2.6. Performance evaluation

Fig. 5 presents the prototype of the constructed motor with the stator core made by the alloy Fe–Co and the rotor with NdFeB permanent magnets. Two experiments were conducted to examine the performance of the motor; one was performed by setting the armature current to be 800 mA and altering the rotor's angles, and the other was carried out by changing the armature current but keeping the rotor at a fixed constant angle, for example, 40°. Fig. 6 depicts the experimental torque of the designed motor over the limited rotor's angles and the relationship of torque and the armature current. The minimum and maximum torque outputs of the motor are about 1.37 kg cm and 1.43 kg cm, respectively. In Fig. 6, although the experimental torque outputs are less than the simulated ones, the experimental result showed a high degree of consistence with the predicted one. Fig. 6a also shows that when the armature current is 800 mA, the total resultant electromagnetic torque of the motor is approximately obtained from Eq. (6), and the torque remains almost constant within the limited rotor's angles from −60° to 60°. This result clearly confirms the validity of the torque equation (6). Moreover, the result in Fig. 6b shows that the approximate torque equation (6) is correct and useful, namely that the torque equation (6) is shown valid, the generated torque is proportional to the armature current, and independent of the rotor's positions. Worthy of mention is that although the result in Fig. 6b was obtained from the second experiment, it can be further verified by conducting the same experiment with different rotor's angles.

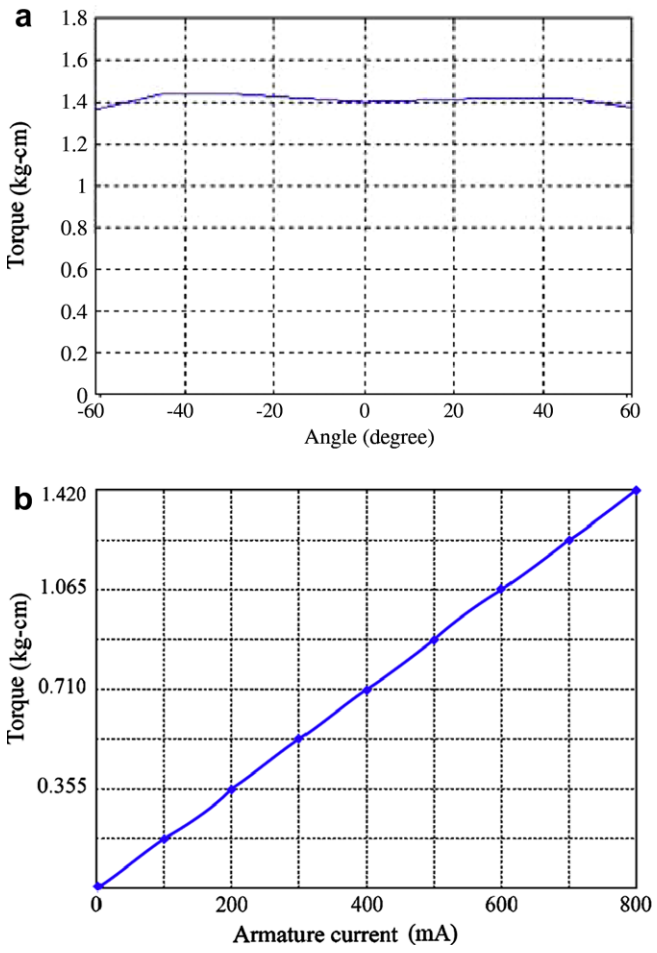

Fig. 6. (a) Experimental motor torque over the limited rotor's angles when the armature current is 800 mA. (b) Plot of torque versus armature current for the designed motor.

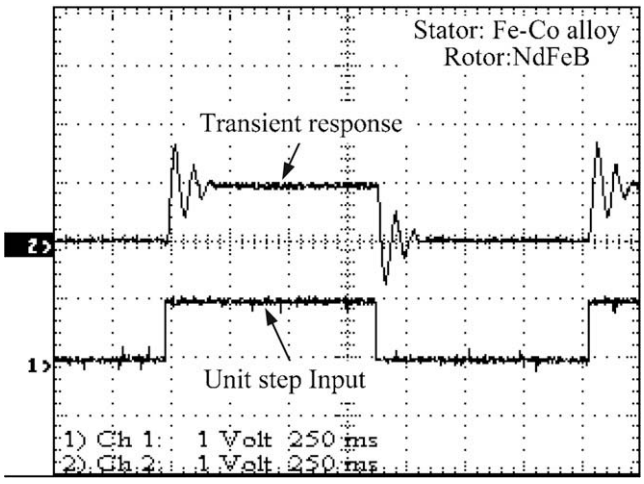

Fig. 7. Step response of the built motor using analog proportional position control.

To further investigate the dynamic behavior of the proposed motor, Fig. 7 depicts the step-like set-point transient response of the designed motor using an analog proportional position controller with its proportional gain of 0.3. The unit step input means the input reference of 1 VDC, and the transient response represents the time behavior of actual position of the controlled motor. In control terminology, such a transient response can be used to find a dynamic model of the motor. Furthermore, the result in Fig. 7 reveals that the analog P controller with gain 0.3 was poor for obtaining satisfactory closed-loop transient response because the closed-loop positioning response had a significant maximum overshot and long settling time. Nevertheless, the experimental response with respect to the kind of input reference will be employed to establish an approximate transfer function of the motor.

In the sequel a two-degree-of-freedom position controller will be synthesized in the following section to improve the bad dynamic response of the torque motor while applied to small-scale gas turbine engine fuel control.

3. Application to fuel control of a small-scale gas turbine engine

3.1. Brief description of the small-scale gas turbine fuel system

This subsection aims to briefly describe the fuel control system of a small-scale gas turbine engine where the fuel flow rate is the ultimate controlled variable. Fig. 8 shows the physical configuration of a typical fuel control system in a small-scale gas turbine engine, where the controlled fuel flow rate at the outlet of the system

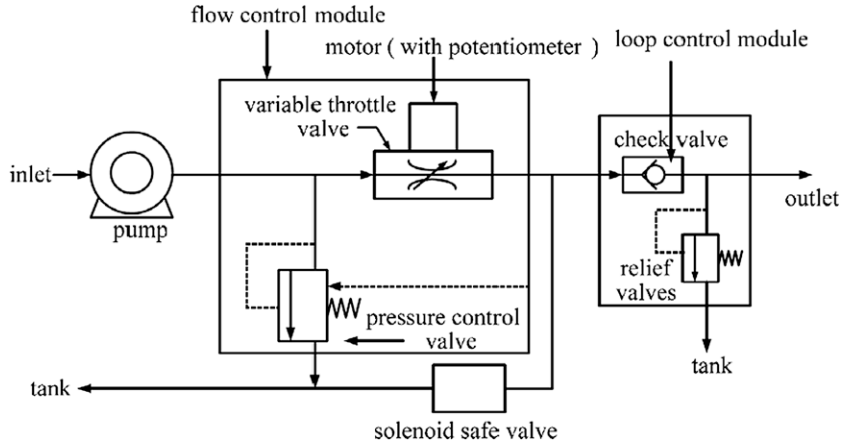

Fig. 8. Physical configuration of a typical small-scale gas turbine fuel system.

directly affects the propulsion power of the small-scale gas turbine engine. The torque motor is directly connected to the variable-throttle valve where the opening degree (area) of the orifice controls the fuel flow rate into the small-scale gas turbine engine. The pressure control valve is employed to ensure that the differential hydraulic pressure between the inlet and the outlet of the variable-throttle valve is constant. The safe valve is a protection device to prevent the pressure from dangerous level tolerance. The loop control module makes sure that fuel flows to the spray nozzle at a specified direction. In the following, the nonlinear properties of the pressure control valve and the variable-throttle valve will be briefly introduced. The pressure control valve is used to maintain the differential pressure between the inlet and outlet of the variable-throttle valve. Thus, the flow rate Q of the fuel valve is described by

$$Q = C_d \cdot A(\theta) \cdot \sqrt{\frac{2}{\rho}(P_i - P_o)} = C_d \cdot A(\theta) \cdot \sqrt{\frac{2}{\rho}\Delta p} \tag{7}$$

where C_d is the orifice discharge coefficient, ρ is the density of the fuel, P_i represents the inlet pressure, P_o the outlet pressure, and Δp is the differential pressure between the inlet and outlet. Assuming that Δp be kept constant due to the pressure control valve, then the flow rate depends on the open area $A(\theta)$. The variable-throttle valve is directly mounted on the torque motor. The open area A of the orifice on the valve is the function, $A(\theta)$, of the rotary angle θ of the torque motor. Notice that the function $A(\theta)$ depends upon the shape of the valve. Fig. 9 shows the nonlinear relationship between the flow rate and the opening percentage (area) of the valve, where the differential pressure Δp is made constant via the pressure control valve. Note that a constant load torque about 0.8 kg cm was applied to the valve during experimentation and this torque profile was provided using a small dynamometer. The result in Fig. 9 also indicates the static or steady-state relationship between the flow rate and the opening percentage of the valve.

3.2. Fuel controllers design

The main design idea of the overall fuel controller is to achieve consistent performance of the fuel control system in spite of parameter variations occurring in the proposed LATM and exogenous disturbances. In this subsection, a multi-loop control scheme is employed to accomplish such a control goal by introducing an inner loop, called robust position control loop, to overcome the parameter variations, and an outer loop to carry out the flow rate control with desired performance without any steady-state tracking errors. The inner loop is composed of a feedforward controller (prefilter) and a PID controller, aiming at obtaining robustly and consistently transient responses of the motor in the presence of uncertainties and disturbances. The outer loop, consisting of a simple PI controller and a flow meter, is used to obtain an almost linear relation between the flow rate commands and actual flow rates. It is worth mentioning that if the inner loop is employed without the outer loop, then the fuel control system still works but gives an imperfect linear input–output relationship; however, this kind of semi-closed-loop fuel control policy provides an

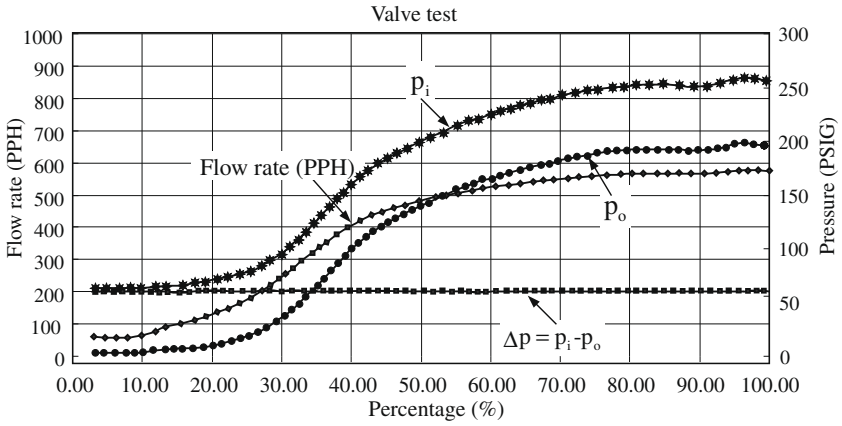

Fig. 9. Flow rate characteristics of the variable throttle valve.

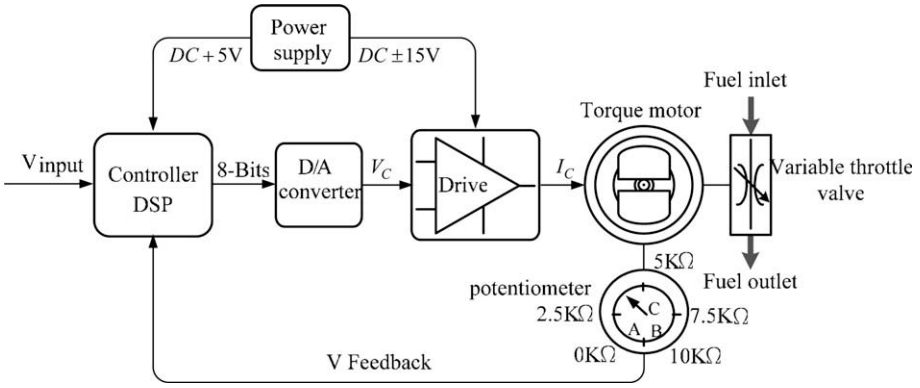

Fig. 10. Block diagram of the proposed semi-closed-loop fuel control system.

inexpensive implementation due to no additional flow meter. On the other hand, for some applications which require precise fuel control, then the closed-loop PI fuel controller associated with the cascaded position control structure and a flow meter is then proposed to accomplish almost linear input–output relationship. However, this closed-loop fuel controller is designed at the cost of an expansive flow meter.

3.3. Semi-closed-loop fuel control

Fig. 10 depicts the block diagram of the semi-closed-loop fuel control system for the small-scale gas turbine engine, in which the inner control loop (robust position control loop for the motor) is employed without consideration of flow dynamics and nonlinear characteristics of the variable throttle valve. The use of the robust motor position control system is necessary to provide the required positioning performance for the developed motor, thereby achieving the simple and inexpensive fuel control. Although giving the nonlinear steady-state relationship between the fuel flow rates and the fuel input commands (see Fig. 18), this simple fuel controller can be applicable to some kinds of small-scale gas turbine engines that requires low-cost fuel control system. In these applications where only the inner control is needed, the prefilter has to be introduced in order to cancel out the system zero(s) such that the resultant LATM position controller is capable of obtaining desired robust set-point tracking performance for the motor.

3.3.1. DSP-based LATM position control system

The DSP-based position control system for the proposed LATM is shown in Fig. 10, where the main controlled variable is the shaft position θ of the torque motor. The potentiometer transforms the shaft position into the voltage used for feedback for the controller. Thus, the negative feedback path constitutes a closed loop for the control system. The single-chip DSP (TMS320F240) from Texas Instruments is responsible for executing all the synthesized control actions; accordingly, the controller has to continuously monitor the feedback voltages from the potentiometer as well as the input position commands. Furthermore, the controller uses the digital-to-analog converter to convert the parallel 8-bit digital signals into the corresponding analog control voltage, and the control voltage is linearly transformed into the driving current for the torque motor by the driving circuitry.

3.3.2. Motor driving circuitry

The type of motor driving circuit is a current-boosted voltage-to-current circuit as shown in Fig. 11a. This circuitry uses the negative feedback principle to achieve an almost linear voltage-to-current relationship. The main function of two power transistors, Q1 and Q2, is to amplify the output current to the torque motor such that the motor is controlled in the current mode. Fig. 11b displays the experimental result of the static voltage-to-current relationship. The result in Fig. 11b presents that the driving module is linear except the saturation regions.

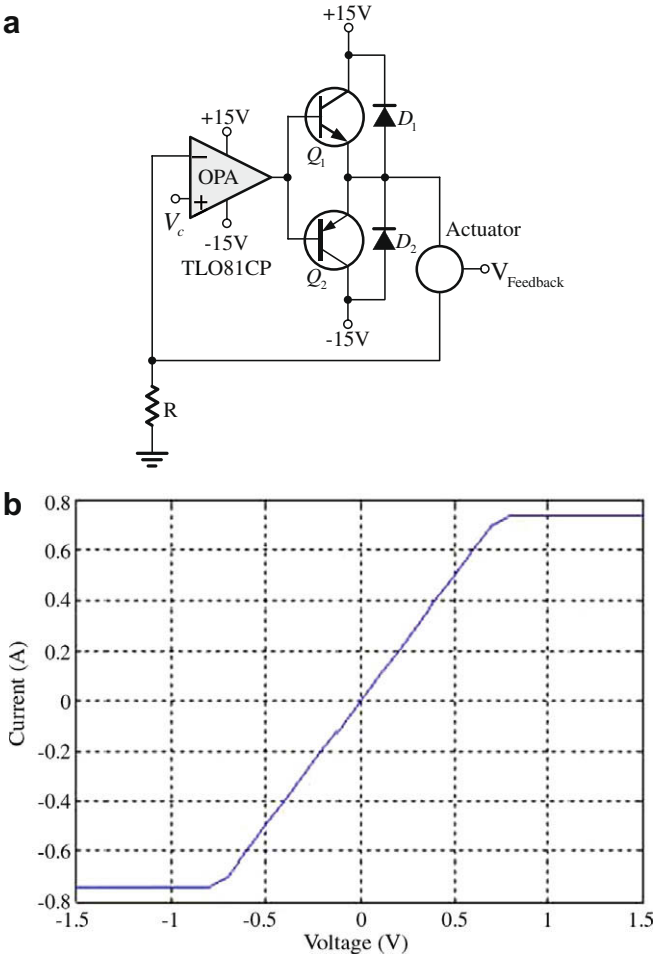

Fig. 11. (a) The proposed driving circuit. (b) The static voltage-to-current relationship.

3.3.3. Experimental modeling of the torque motor

This subsection is devoted to finding an approximate transfer function of the torque motor from experimental data. As can be

seen in Fig. 7, the dynamic behavior of the simple feedback control system with analog proportional position control indeed exhibited an approximately second-order system response, which can be modeled by following second-order transfer function

$$T(s)=\frac{\omega_n^2}{s^2+2\xi\omega_n s+\omega_n^2},\quad 0<\xi<1\quad\text{and}\quad\omega_n>0 \tag{8}$$

By using the experimental data from the step response from Fig. 7, the damping ratio ξ and the natural frequency ω_n are obtained from measurements of the maximum overshot and the settling time, that is,

$$M_p=e^{-\pi\xi/\sqrt{1-\xi^2}} \tag{9}$$

$$t_r=\frac{\pi-\tan^{-1}\frac{\sqrt{1-\xi^2}}{\xi}}{\omega_n\sqrt{1-\xi^2}} \tag{10}$$

As Fig. 9 shows, the maximum overshoot M_p is 0.64 and the rising time t_r is 21.8 ms and the proportional gain, K_P, of the analog controller is 0.3. With the data, the closed-loop transfer function can be then found by

$$T(s)=\frac{K_PG(s)}{1+K_PG(s)}=\frac{2043}{s^2+12.71s+2043} \tag{11}$$

which leads to the open-loop transfer function of the torque motor

$$G(s)=\frac{T(s)}{K_p(1-T(s))}=\frac{2043}{0.3(s^2+12.71s)}=\frac{6810}{s(s+12.71)} \tag{12}$$

3.3.4. Robust position controller design

The basic structure of the proposed robust position control system for the LATM is shown in Fig. 12 in which $R(s)$ represents the reference input of the closed-loop fuel control system, $U(s)$ the output of the compensator $G_c(s)$, $D(s)$ exogenous disturbance in the control system, and $C(s)$ the output of the close-loop fuel control system. The designed objective is to select a prefilter $G_p(s)$ and a compensator $G_c(s)$ in a two-degree-of-freedom feedback configuration so that the transient, and steady state, and frequency domain specifications are satisfied. In addition, the controller design must meet the bandwidth requirement and to prevent the unavoidable measurement noise from degrading the control performance or giving saturation at the stage of $G_c(s)$ or at the early start-up stage. The proposed robust position control system is based on a special type of performance index as in (13) to select the three PID coefficients [24].

$$\text{ITAE}=\int_0^\infty t|e(t)|dt \tag{13}$$

where the performance index is designated the Integrated Time multiplied by Absolute Error, abbreviated by ITAE. This ITAE performance index is used to reduce the contribution of the large initial errors to the value of the performance integral, as well as to emphasize errors occurring large in the response. The ITAE performance criterion for any step input has been employed to determine the optimal coefficients of the following general nth-order closed-loop transfer function [24]

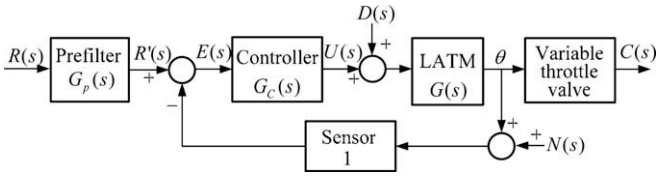

Fig. 12. Block diagram of the robust position control system.

$$T(s)=\frac{C(s)}{R(s)}=\frac{b_0}{s^n+b_{n-1}s^{n-1}+\cdots+b_1s+b_0}$$

which gives a zero steady-state error for a step input. For example, for the third-order closed-loop transfer function, its characteristic equation with the best coefficients determined by the ITAE criterion is $s^3+1.75\omega_ns^2+2.15\omega_n^2s+\omega_n^3=0$ in which the natural frequency ω_n is obtained from the specification of settling time. Next, the aforementioned technique will be applied to find the robust position controller, which is composed of a PID controller and a prefilter. Given the PID controller

$$G_c(s)=\frac{K_ds^2+K_ps+K_i}{s} \tag{14}$$

where K_d, K_p and K_i are the three-term parameters, the closed-loop transfer function without the prefilter $T'(s)$ is given by

$$T'(s)=\frac{C(s)}{R'(s)}=\frac{G_cG(s)}{1+G_cG(s)}=\frac{6810(K_ds^2+K_ps+K_i)}{s^3+(12.71+6810K_d)s^2+6810K_ps+6810K_i} \tag{15}$$

By choosing ω_n = 50 rad/s to meet the bandwidth requirement, one obtains the optimum coefficients of the third-order characteristic equation for ITAE by

$$s^3+87.5s^2+5375s+125000=0 \tag{16}$$

Equating the denominator of (15), (16) yields the three-term coefficients K_p = 0.7893, K_i = 18.3554, and K_d = 0.011. To achieve the desired ITAE response, it requires that the overall transfer function from the input R(s) to the output C(s) becomes

$$T(s)=\frac{C(s)}{R(s)}=\frac{G_pG_cG(s)}{1+G_cG(s)}=\frac{125000}{s^3+875s^2+5375s+125000} \tag{17}$$

From (17), the prefilter is obtained from

$$G_p(s)=\frac{1671.3464}{s^2+71.754s+1671.3} \tag{18}$$

which cancels out the zero in (15) and makes the overall system become a unity-gain system. This completes the design of the robust position controller for the LATM. Computer simulation results show that the robust position controller generates small overshoots of 1.9%, desired rising time of 0.04 s and settling time of 0.14 s for a unit step disturbance, and the maximum value of $C(t)/D(t)$ due to the disturbance is 0.08%, showing satisfactory disturbance rejection capability. Note that, to obtain desired transient responses for any step-like position setpoints, the prefilter must be employed to cancel out the two system zeros form the PID controller in the feedback loop. If these two system zeros are not cancelled out by the prefilter, the overall position control loop will have a very oscillatory transient response whose percentage of maximum overshoot can be up to 36.5%.

3.4. Closed-loop fuel controller design with a flowmeter

The design of the previous semi-closed-loop fuel control system is easy and simple, but at the cost of the nonlinear input–output relationship between the fuel rate command and the actual fuel flow rate. This is in part due to the nonlinear variable-throttle value, and in part because of no flow transducer for measuring the fuel flow rate. Moreover, another drawback of the previous semi-closed-loop fuel controller is that its overall set-point step tracking performance varies with the input fuel rate commands. To overcome the shortcoming, this subsection aims at designing a feedback controller with a flowmeter, and the control objective is to have the linear relationship between the input fuel rate command and the output fuel flow rate. Fig. 13 illustrates the block diagram

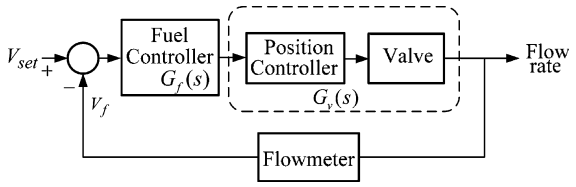

Fig. 13. Block diagram of the closed-loop fuel control system with a flow meter.

of the closed-loop fuel control system with a flowmeter. As shown in Fig. 13, the transfer function $G_v(s)$ indeed represents an approximation of the closed-loop transfer function of the inner position control loop and flow dynamics. To proceed with the approximate modeling process, it is necessary to conduct several experiments to obtain transient responses of the transfer function $G_v(s)$ for the following four cases: (1) $V_{set} = 0.5$ V; (2) $V_{set} = -0.5$ V; (3) $V_{set} = -1.0$ V; (4) $V_{set} = -1.5$ V. Fig. 14a–d depicts the four set-point tracking responses. From the experimental data, the transfer functions for the four cases are experimentally obtained as follows; (1) $G_{v1} = \frac{9.92}{s+5.95}$; (2) $G_{v2} = \frac{6.709}{s+5.81}$; (3) $G_{v3} = \frac{5.0168}{s+5.81}$; (4) $G_{v4} = \frac{4.276}{s+4.83}$.

Thus, the transfer function of the position control loop and flow dynamics can be given by the following first-order system model:

$$G_v(s) = \frac{K(\theta)}{s + a(\theta)}, \quad 4.83 \leqslant a(\theta) \leqslant 5.95, 4.276 \leqslant K(\theta) \leqslant 9.92 \qquad (19)$$

which has the time-varying parameters and steady-state errors for any set-point input.

Note that the response time of the used flowmeter (Model FT4-6 from FlowMeasurementSystems) is about 4 ms, thereby giving its bandwidth of 250 Hz. In comparison the bandwidth of the inner position control loop along with flow dynamics (about 5–6 rad/s), the dynamics of the flowmeter is much faster and can then be neglected in the controller design.

Since the model (19) has the time-varying parameters and steady-state error for a step input, a PI control policy is employed to achieve the design goal. The transfer function of the overall system is

$$T(s) = \frac{K(K_P s + K_I)}{s^2 + (a + KK_P)s + KK_I} \qquad (20)$$

where the natural frequency ω_n is designed to be smaller than 18 rad/s since ω_n of the inner loop is 50 rad/s. This implies

$$KK_I \leqslant 324 \qquad (21)$$

To complete the controller synthesis, we consider the worst case that $a = 5.95$ and $K = 9.92$. Assume that the desired minimum-damping ratio ζ must be larger than 0.6, and then the selections of K_p and K_I must satisfy the following two inequalities:

$$\begin{cases} 2.26 \leqslant K_i \leqslant 32.6 \\ K_p \geqslant \frac{1.2\sqrt{K_i} - 1.88}{3.15} \end{cases} \qquad (22)$$

Hence, a simple PI fuel controller with the flowmeter is chosen as

$$G_f(s) = 2 + \frac{15}{s} \qquad (23)$$

4. Fuel control experiments, results and discussion

4.1. Experimental setup

Fig. 15 depicts the control architecture of the experimental small-scale gas turbine fuel control system and the prototype of

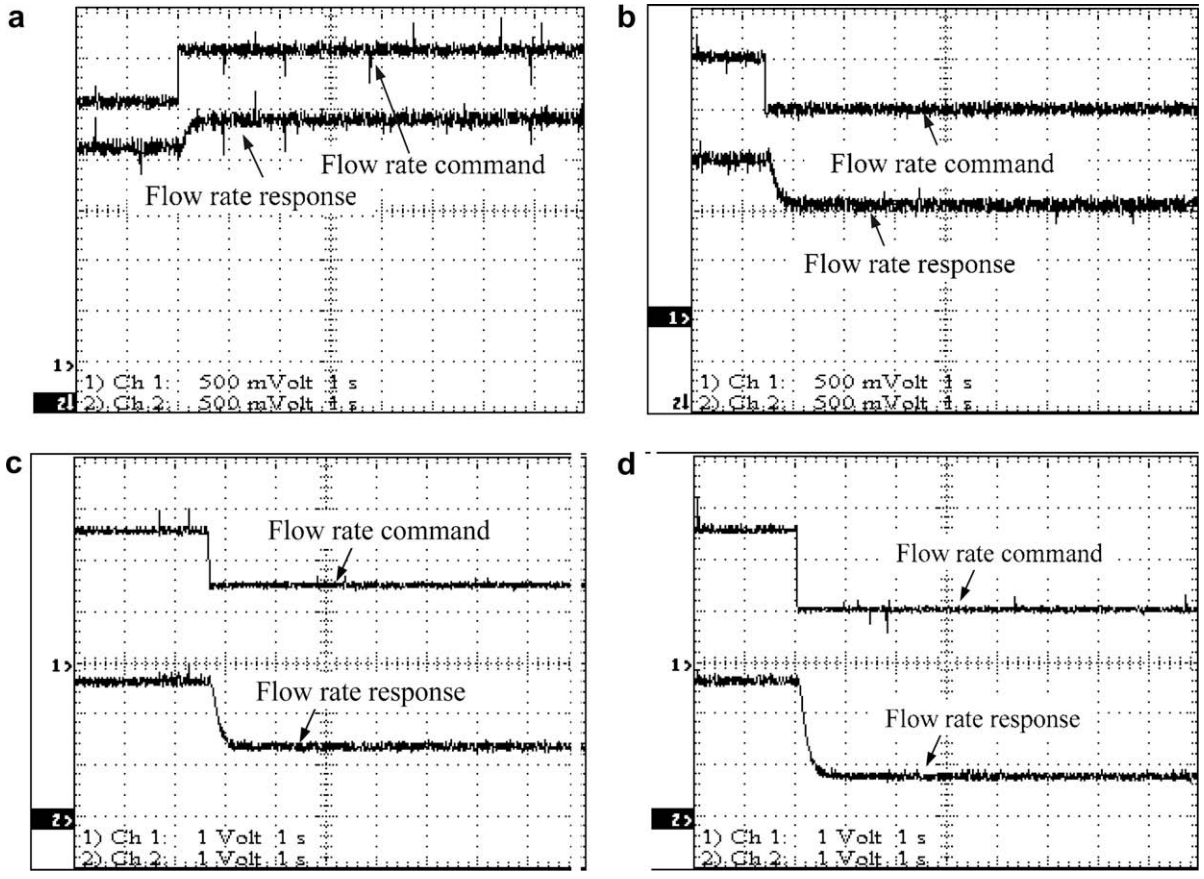

Fig. 14. Flow rate responses for (a) $V_{set} = 0.5$ V; (b) $V_{set} = -0.5$ V; (c) $V_{set} = -1.0$ V; (d) $V_{set} = -1.5$ V.

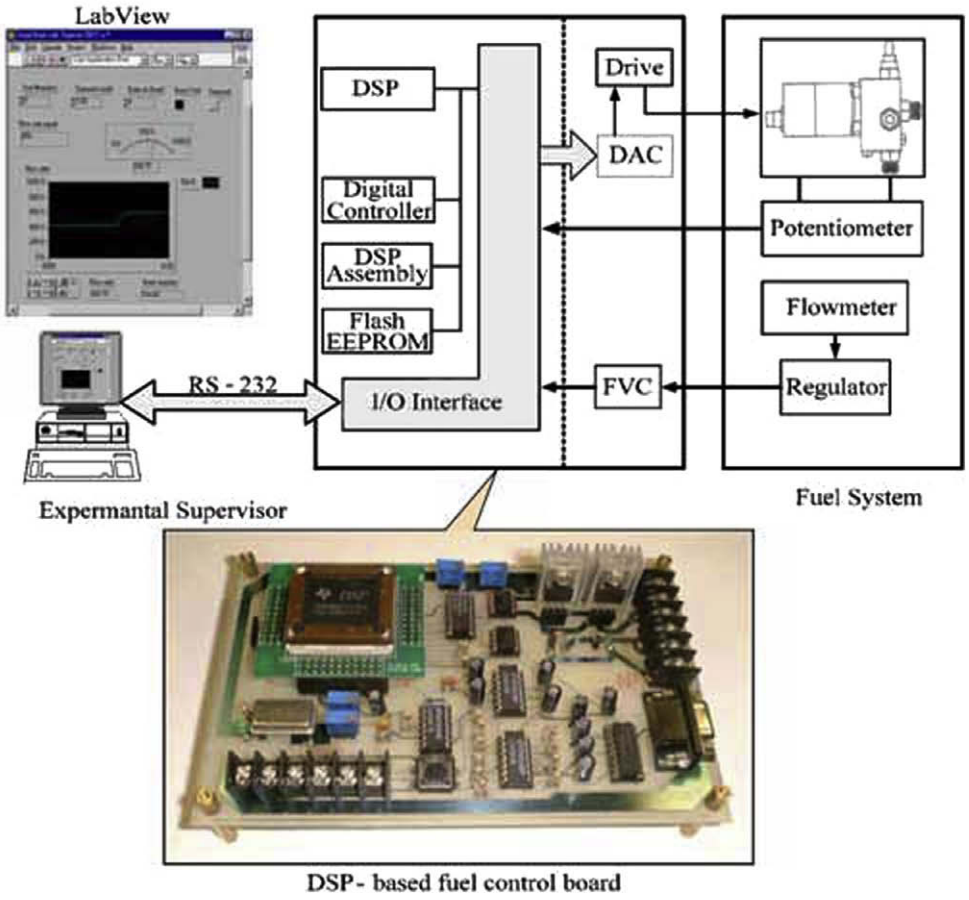

Fig. 15. Monitoring and control architecture of the experimental small-scale gas turbine engine fuel controller.

the DSP-based fuel control board. The robust position controller developed in Section 3.3.4 is considered as the inner loop controller and the closed-loop PI fuel controller is then considered as the outer loop controller. The flow rate signal measured by the flowmeter is a sinusoidal wave of low magnitude, and is amplified and converted to a square wave. The frequency-to-voltage converter (FVC) converts the frequency of the square wave into a corresponding analog voltage. The PI fuel controller performs the closed-loop control using the feedback voltage of the flow rate. Beside, the remote supervisor using LabVIEW can monitor the changes of the variable in the system or manipulate the controlled variable through the serial port. The flow meter has a small fan and

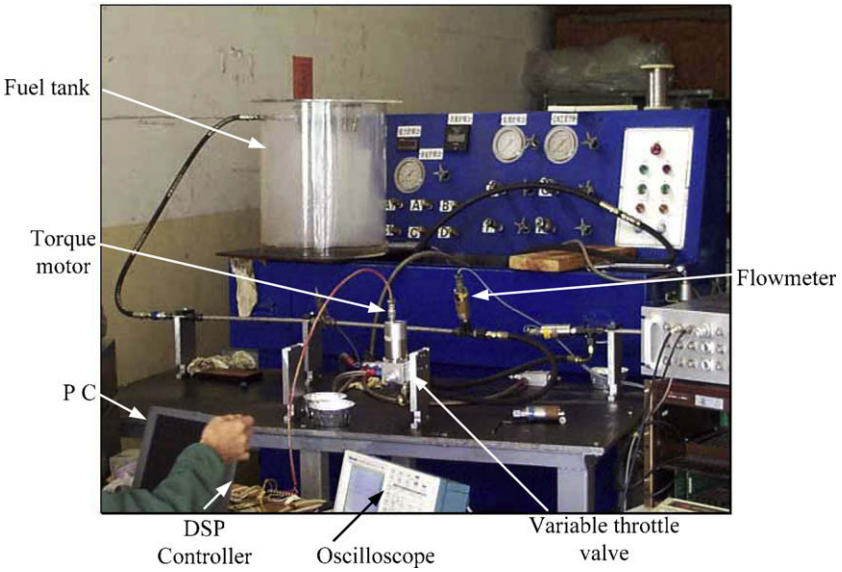

Fig. 16. Picture of the experimental fuel control system.

several induction coils. As the fuel flows through it, the fan generates a rotary movement. This action causes the coils to induce a sinusoidal voltage, which is proportional to the flow rate of the fuel. Fig. 16 depicts the experimental fuel system.

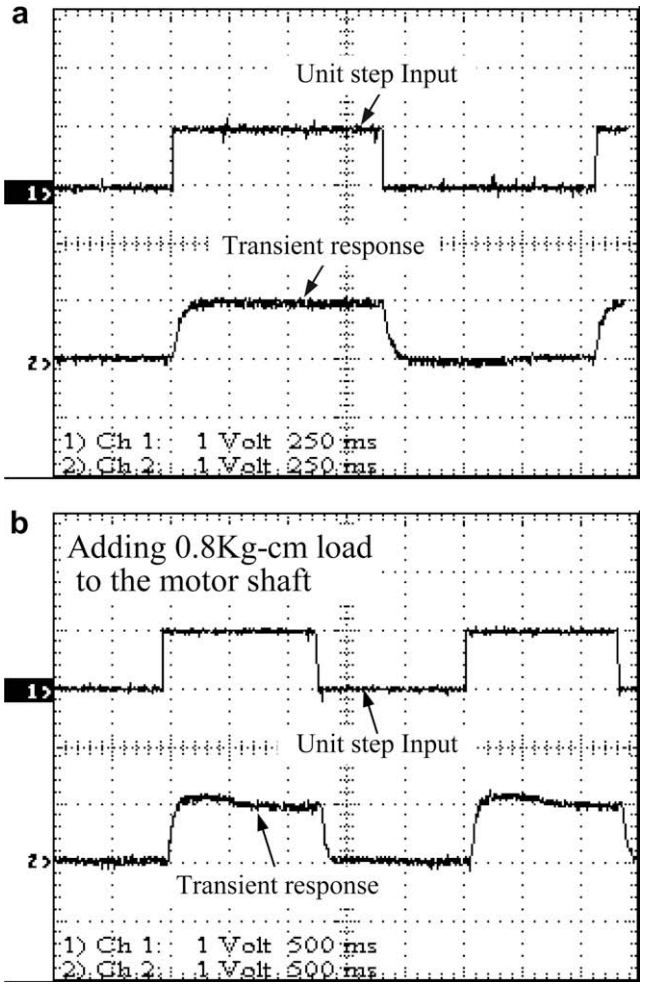

Fig. 17. (a) Unit step response of the controlled torque motor. (b) Unit step response of the controlled torque motor in the presence of external disturbance.

4.2. Semi-closed-loop fuel control experiments

The experiment was conducted to examine and verify the proposed DSP-based robust position controller for achieving semi-closed-Loop fuel control. Fig. 17a depicts the set-point tracking response of the proposed robust position controller whose performance is characterized by the maximum overshoot of 0%, the rising time of 0.04 s, and the settling time of 0.12 ms. The result clearly indicate that the experimental result is highly consistent with the simulation result in Section 3.3.4. Furthermore, adding an extra load torque 0.8 kg cm to the shaft obtained the experimental set-point tracking response, as shown in Fig. 17b. The result in Fig. 17b also reveals that the robust position controller has the excellent disturbance rejection as predicted by the previous numerical simulation. Fig. 18 shows that the kind of fuel controller gives the nonlinear steady-state relationship between the fuel flow rates and the fuel input commands. Notice that the saturation of the fuel control system is unavoidable due to the characteristics of the variable-throttle valve.

4.3. Experimental results of the closed-loop fuel controller with the flowmeter

Fig. 19 shows the transient step response of the fuel controller given in (23) for the worst case. Worthy of mention is that there

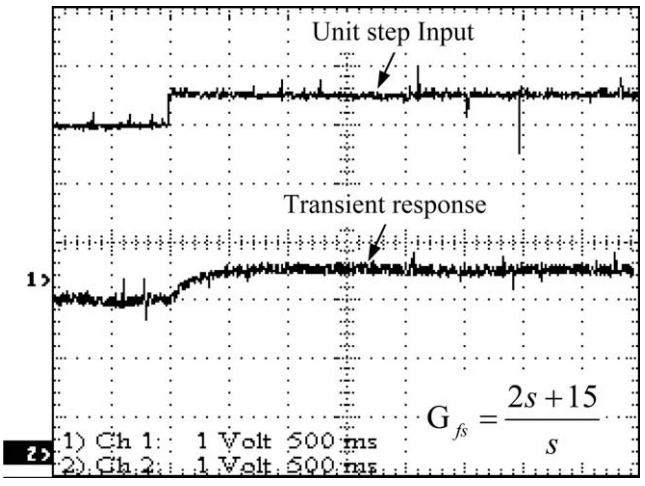

Fig. 19. Experimental closed-loop response of the controlled torque motor with the Setpoint V_{ref} = 1 V.

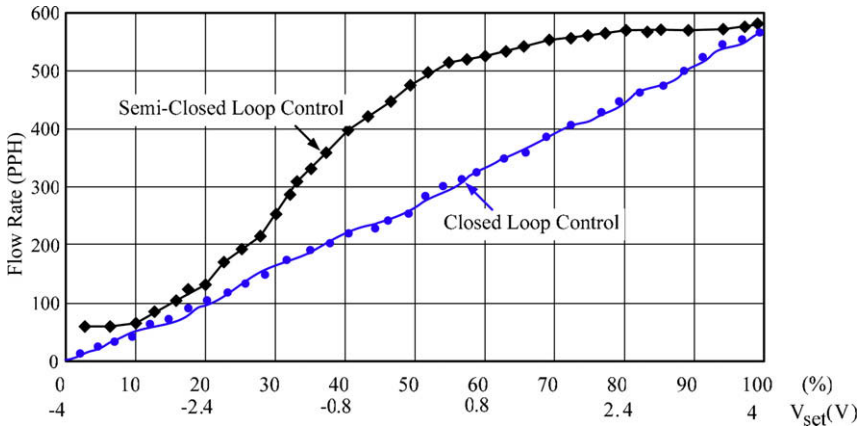

Fig. 18. Comparison of the steady-state flow rate characteristics of the proposed semi-closed-loop controller and closed-loop fuel controller.

are no steady-state errors in Fig. 19. This shows that the performance of the proposed fuel controller with the flowmeter is greatly improved while compared with the semi-closed-loop fuel controller. Fig. 18 compares the steady-state fuel flow characteristics of the two proposed fuel controllers. The results in Fig. 18 indicate that the nonlinearity caused by the semi-closed-loop fuel controller is almost eliminated via the closed-loop feedback policy.

5. Conclusions

This paper has proposed techniques for design and implementation of a brushless DC limited angle torque motor with its application to fuel control of small-scale gas turbine engines. Through FEM-based computer simulations and experimental results, the design strategy of the proposed brushless DC LATM has been confirmed effective and useful in achieving required specifications. The two-degree-of-freedom position controller has been successfully designed and implemented on a DSP chip for the LATM. With the robust position controller, the semi-closed-loop fuel controller is easily developed to accomplish a low-cost fuel supply strategy for small-scale gas turbine engines, but its relationship between the steady-state fuel flow rates and their commands remains nonlinear. Therefore, the closed-loop fuel controller with a flow meter is then synthesized to accomplish desired linear relationship. The experimental results have shown that the closed-loop fuel controller overcomes the plant uncertainties and nonlinearity. In comparison with both proposed fuel control approaches, the semi-closed-loop fuel controller is much more inexpensive than the closed-loop fuel controller, but the latter outperforms the former in terms of transient responses and steady-state characteristics. An interesting topic for future research might be to design a linear throttle valve so as to greatly reduce the design complexity and cost of the fuel controller.

Acknowledgements

The authors acknowledge financial support in part from the National Science Council of the Republic of China under Grant NSC 89-CS-D-005-001, and in part from the Ministry of Education, Taiwan, under the ATU plan.

References

[1] Dawson C, Bolton HR. Performance prediction of a wide-angle limited-motion rotary actuator. Proc Inst Elect Eng, Part B 1978;125(9):895–8.
[2] Dawson C, Bolton HR. Design of a class of wide-angle limited-motion rotary actuators. Proc Inst Elect Eng Part B 1979;126(4):345–50.
[3] Dawson C, Bolton HR. Limited-motion rotary actuators of toroidal-stator, permanent-magnet rotor type. Proc Inst Elect Eng, Part B 1982;129(4):190–8.
[4] Zhang Y, Smith IR, Kettleborough JG. Performance evaluation for a limited-angle torque motor. IEEE/ASME Trans Mechatron 1999;4(3):335–9.
[5] Krishna PM, Kannan N. Brushless DC limited angle torque motor. In: Proceedings of the 1996 international conference on power electronics, drives and energy systems for industrial growth, vol. 1; 1996; p. 511–6.
[6] Du CY, Li T, Cao ZC. Accurate tracking control of a limited angle torque motor. In: Proceedings of the conference record of the 38th IEEE IAS annual meeting and industry applications, vol. 2; 2003. p. 744–8.
[7] Rao AS. Alnico permanent magnets and overview. In: Proceedings of the electrical electronics insulation conference and electrical manufacturing & coil winding conference; 1993. p. 373–83.
[8] Tufts CR. Selecting the correct magnetic material. In: Proceedings of the electrical electronics insulation conference; 1995. p. 65–8.
[9] Mhango LMC. Benefits of Nd–Fe–B magnet in brushless DC motor design for aircraft applications. In: Proceedings of the fourth international conference on electrical machines and drives; 1989. p. 76–9.
[10] Petrie R. Permanent magnets in review. In: Proceedings of the electrical electronics insulation conference and electrical manufacturing & coil winding conference; 1993. p. 207–10.
[11] Pal SK. Comparative study of the design and development of direct drive brushed and brushless DC motors with samarium cobalt, neodymium–iron–boron and ceramic magnets. IEE Colloquium on Permanent Magnet Machines and Drives 1993:711–7.
[12] Oman H. Permanent magnets for vehicle-propulsion motors: cost/availability. In: Proceedings of the energy conversion engineering conference, vol. 1; 1996. p. 91–6.
[13] Jabbar MA, Low TS, Rahman MA. Permanent magnet motors for brushless operation. IEEE Trans on Ind Appl 1990;26:124–9.
[14] Yoon T. Stator design consideration of a brushless DC motor for robust rotor position detection in inductive sense start-up. IEEE Trans Magn 2006;42(3):453–9.
[15] Zheng L, Wu TX, Acharya D, Sundaram KB, Vaidya J, Zhao L, et al. Design of a super high-speed cryogenic permanent magnet synchronous motor. IEEE Trans Magn 2005;41(10):3823–5.
[16] Komori M, Yamane T. Magnetic levitation system with a millimeter-sized cylindrical rotor. Mechatronics 2000;10:595–607.
[17] Pinhas BT, Mrad RB, Goldenberg AA. A conceptual design and FE analysis of a piezoceramic actuated dispensing system for microdrops generation in microarray applications. Mechatronics 2007;17:1–13.
[18] Gair S, Canova A, Eastham JF, Betzer T. A new 2D FEM analysis of a disc machine with offset rotor. In: Proceedings of the 1996 international conference on power electronics, drives and energy systems for industrial growth, vol. 1; 1996. p. 617–21.
[19] Hanselmann H. DSP in control: the total development environment. In: Proceedings of the 1996 IEEE IECON 22nd international conference on industrial electronics, control, and instrumentation, vol. 3; 1996. p. 1647–54.
[20] Choi C, Tsao TC. Control of linear motor machine tool feed drives for end milling: Robust MIMO approach. Mechatronics 2005;15:1207–24.
[21] Brown MN, Stewart RW, Durrani TS. DSP subsystem for knowledge based health monitoring of gas turbine engines. In: Proceedings of the IEEE international conference on acoustics, speech, and signal processing, vol. 5; 1992; p. 69–72.
[22] Exley TJ. Low cost propulsion for unmanned air vehicles. American Institute of Aeronautics and Astronautics paper 1991;29:2559.
[23] Nikkhajoei H, Iravani MR. A matrix converter based micro-turbine distributed generation system. IEEE Transactions on Power Delivery 2005;20(3):2182–92.
[24] Dorf RC, Bishop RH. Modern control systems. 10th ed. New York: Prentice-Hall; 2005.